Hybrid DFT calculation of ^{57}Fe NMR resonances and orbital order in magnetite

C. H. Patterson
School of Physics, Trinity College Dublin, Dublin 2, Ireland
(Received 4 July 2014; revised manuscript received 5 August 2014; published 20 August 2014)

The crystal structure and charge and orbital order of magnetite below the Verwey temperature are calculated using a first-principles hybrid density functional theory (DFT) method. The initial atomic positions in the crystal-structure calculation are those recently refined from x-ray diffraction data for the Cc space-group unit cell [Senn, Wright, and Attfield, Nature (London) **481**, 173 (2012)]. Fermi contact and magnetic dipolar contributions to hyperfine fields at ^{57}Fe nuclei obtained from hybrid DFT calculations are used to obtain NMR resonance frequencies for magnetite for a range of external magnetic field directions in a relatively weak field. NMR frequencies from hybrid density functional theory calculations are compared to NMR data [M. Mizoguchi, J. Phys. Soc. Jpn. **70**, 2333 (2001)] for a range of applied magnetic field directions. NMR resonance frequencies of B-site Fe ions show large relative variations with applied field direction owing to anisotropic hyperfine fields from charge and orbital ordered Fe $3d$ minority-spin electrons at those sites. Good agreement between computed and measured NMR resonance frequencies confirms the pattern of charge and orbital order obtained from calculations. The charge and orbital order of magnetite in its low-temperature phase obtained from hybrid DFT calculations is analyzed in terms of one-electron bonds between Fe ions. The Verwey transition in magnetite therefore resembles Mott-Peierls transitions in vanadium oxides which undergo symmetry-breaking transitions owing to electron-pair bond formation.

DOI: 10.1103/PhysRevB.90.075134 PACS number(s): 61.50.Ah, 75.47.Lx, 75.50.Gg

I. INTRODUCTION

The crystal structure and associated charge and orbital order of magnetite below the Verwey transition temperature, $T_V \sim 120$ K, have been the subject of numerous experimental and theoretical studies since the discovery of the transition in 1939 [1]. Resonant x-ray diffraction (RXRD) has been used to probe charge and orbital order in magnetite [2–9], but no conclusive picture of charge and orbital order in magnetite has emerged from RXRD. The Verwey transition has also been probed using infrared and Raman spectroscopies [10]. A ^{57}Fe Mössbauer spectroscopy study of magnetite across the Verwey transition [11] found no evidence of charge separation at T_V on the Mössbauer time scale. Superconducting quantum interference device (SQUID) measurements of magnetization of magnetite below T_V have found a saturation magnetic moment in the range of $4.1\mu_B$ [12] to $4.3\mu_B$ [13], implying that there is some orbital contribution to the magnetic moment. However, a spin-dependent Compton scattering study concluded that the orbital contribution to the magnetic moment is less than $0.1\mu_B$ [14].

Recent x-ray diffraction (XRD) structure refinements for the phase below T_V have used $P2/c$ [15], $C2/c$ [16], and Cc [17] space groups. The observed space group of magnetite below T_V is Cc. Extensive twinning of the unit cell, which has a monoclinic angle close to 90° (90.236°) [17], has complicated the solution of the crystal structure of magnetite below T_V. The study by Senn and coworkers [17] used a 40-μm grain with one dominant domain to obtain the structure in the actual unit cell and space group. Density functional theory + Hubbard's U (DFT + U) and hybrid DFT methods have been applied to the problem of charge and orbital order of magnetite below T_V using both $P2/c$ [18–21] and Cc [20–23] space-group representations of the crystal structure. Hereafter, magnetite in the Cc unit cell is referred to as Cc magnetite.

Magnetite, Fe_3O_4, has an inverse spinel structure, AB_2O_4, which formally has Fe^{3+} ions on A sites tetrahedrally coordinated by O ions and equal proportions of Fe^{3+} and Fe^{2+} on octahedrally coordinated B sites. The Cc unit cell of magnetite has eight unique Fe A sites and 16 unique B sites, each of which is symmetry related to one other site by a glide plane parallel to the conventional unit-cell ac plane. B-site ions form a tetrahedral network, and there are eight tetrahedra types in the Cc unit cell (Fig. 1).

The Verwey transition is a metal-insulator transition in which the conductivity changes by two orders of magnitude [1]. It is accompanied by symmetry breaking from a cubic $Fd\bar{3}m$ space-group structure with 2 formula units per primitive cell to a monoclinic Cc structure with 16 formula units. Verwey's original conception of charge order in magnetite [24] was freezing of rapid exchange of minority-spin $3d$ electrons between B sites into ordered Fe^{2+} and Fe^{3+} ions.

The results of first-principles calculations presented here strongly support an alternative viewpoint for minority-spin charge distribution in magnetite which accounts for intermediate valence of B sites. Sixteen minority-spin $3d$ electrons in the Cc magnetite primitive unit cell are shared between neighboring B sites and form one-electron bonds between those sites. One-electron bonds were first described by Pauling [25]. They exist only between homonuclear species but can be quite strong. For example, the binding energy in the hydrogen molecular ion is 2.8 eV [26]. In Cc magnetite one-electron bonds form when Fe B-site t_{2g} orbitals are aligned, so that they overlap to the greatest extent (Fig. 2). This interaction shortens distances between ions where a bond is formed.

Recent measurements of short-range charge correlations in magnetite above T_V [27] follow earlier work on diffuse neutron scattering, which was interpreted in terms of scattering by molecular polarons [28,29]. These correlations may be caused by sharing of single electrons between Fe ions in one-electron

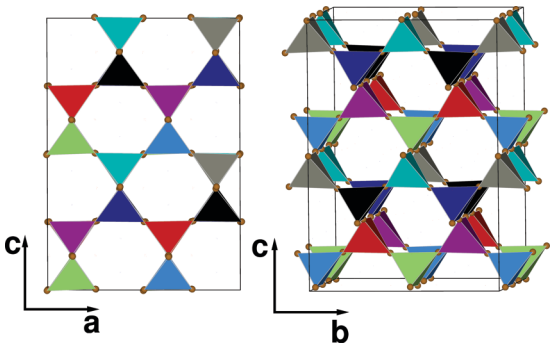

FIG. 1. (Color online) Arrangement of eight distinct Fe tetrahedra in the conventional unit cell of Cc magnetite. B-site Fe ions are represented as brown spheres. Each color represents a distinct quasitetrahedral arrangement of Fe-Fe distances.

bonds. Figure 2 shows a molecular polaron coordinate similar to that used to account for diffuse neutron scattering patterns [29]. Sharing of minority-spin electrons between sites in mixed valence magnetite in this way leads to lattice distortion. It is reminiscent of electron pairing in metal-insulator transitions in vanadium oxides such as VO_2 [30–35]. There the electronic configuration of V^{4+} ions changes markedly at the transition temperature [33], and pairing of V $3d$ electrons on neighboring sites to form electron-pair bonds leads to a Peierls-Mott distortion and band gap opening at 342 K [32,34,35].

NMR is uniquely suited to probing charge and orbital order in magnetite. ^{57}Fe is a spin-1/2 nucleus and is sufficiently abundant (2%) to be used for NMR measurements. Orbitally ordered minority spins on B sites produce anisotropic hyperfine fields at ^{57}Fe nuclei, which can be probed by measuring NMR spectra as a function of applied magnetic field direction in a single crystal. The degree of hyperfine anisotropy at a particular Fe site depends on occupation of the minority-spin Fe $3d$ orbitals at that site and dipolar fields from neighboring sites. NMR frequencies from A sites are expected to be only weakly dependent on crystal orientation in an external field. The Fe^{3+} ion has a $^6S_{5/2}$, spherically symmetric ground-state electronic configuration in free space, whose shape is expected to be similar in a crystalline environment. An entirely spherical electronic distribution implies zero anisotropy in the hyperfine

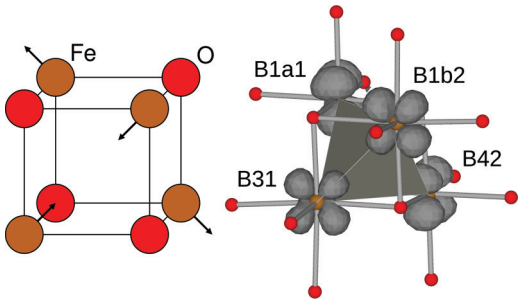

FIG. 2. (Color online) (left) Molecular polaron coordinate leading to shortening and lengthening of Fe-Fe distances and (right) orbital order about one Fe_4 tetrahedron where a one-electron bond has formed between Fe B31 and Fe B1b2. The labeling scheme for Fe ions is described in the text.

field at the nucleus. In that case only the Fermi contact hyperfine field contributes to the NMR resonance frequency, in the absence of an external magnetic field. The NMR spectrum of magnetite has been measured in the temperature range 4.2 to 135 K [36] using a spin-echo technique with no external field. In this case the magnetization is expected to align with the easy axis of magnetite [12] (c axis) below T_V. A subsequent NMR study [37], in which the spectrum was measured with a 1.3-T external field oriented in conventional unit-cell ac, bc, and ab planes, showed considerable hyperfine field anisotropy for B sites and weak anisotropy for A sites, as expected for a state with orbital order on B sites only.

Here, isotropic Fermi contact and anisotropic magnetic dipolar terms in the Hamiltonian for magnetite are calculated using the charge and orbital ordered state obtained using the XRD structure from Senn and coworkers [17] and the structure which results when this is relaxed using hybrid DFT. NMR resonance frequencies are calculated as a function of external field direction. NMR resonances measured by Mizoguchi in a spherical single crystal of magnetite [37] as a function of external magnetic field direction for each of the 8 A and 16 B sites in the Cc unit cell are assigned to specific Fe ions using these calculations. Good agreement between theory and experiment, in terms of the numbers of ions with specific variations and splittings of frequencies as a function of crystal orientation in an external field, demonstrates that the charge and orbital order found in hybrid DFT calculations is correct. It is worth noting that the charge and orbital order found by DFT calculations with the new Cc space-group structure [23] differ markedly from the charge and orbital found with a $P2/c$ space-group unit cell [18–21,38].

In the following sections, assumptions made in calculating NMR resonance frequencies are outlined. The charge and orbital order of Cc magnetite is presented. Methods for calculating Fermi contact hyperfine fields are described, and results for Fe ions are given. Variations of NMR resonance frequencies with magnetic field direction from DFT calculations are compared to Mizoguchi's measurements [37], and the 8 A and 16 B sites in the NMR spectrum of magnetite are assigned. This paper concludes with a discussion of the results presented; the Appendix gives details of calculations. Electronic configurations of Fe ions and electronic band structures are given in the Supplemental Material [39].

II. THEORY

The Hamiltonian adopted in this work for electron and nuclear magnetic moments, μ_S and μ_I, on ^{57}Fe sites,

$$H = H_{ez} + H_{hf} + H_{nz}, \tag{1}$$

includes electron and nuclear Zeeman terms, $H_{ez} = -\mu_S \cdot \mathbf{B}$ and $H_{nz} = -\mu_I \cdot \mathbf{B}$, as well as hyperfine terms [40], H_{hf}, which couple electron and nuclear magnetic spins, $\mathbf{S}$ and $\mathbf{I}$, via

$$H_{hf} = \mathbf{I} \cdot \mathbf{A} \cdot \mathbf{S}. \tag{2}$$

The coupling constant $\mathbf{A}$ contains both an isotropic Fermi contact term,

$$\mathbf{A}_0 = \frac{2\mu_0}{3} g\beta_e g_n \beta_n \rho_{\text{spin}}(0)\mathbf{1}, \tag{3}$$

and an anisotropic dipole-dipole coupling term,

$$\mathbf{A}_1 = \frac{\mu_0}{4\pi} g\beta_e g_n \beta_n \mathbf{T}, \tag{4}$$

where $\mathbf{1}$ is the 3×3 unit matrix and $\mathbf{T}$ is a traceless, symmetric 3×3 tensor,

$$(\mathbf{T})_{ij} = \sum_{\mu\nu\sigma} P_{\mu\nu\sigma} \int d\mathbf{r}\, \phi_{\mu\sigma}(\mathbf{r}) \left(\frac{r^2\delta_{ij} - 3x_i x_j}{r^5} \right) \phi_{\nu\sigma}(\mathbf{r}). \tag{5}$$

g and g_n are the electron and nuclear g factors. β_e and β_n are the Bohr and nuclear magnetons, and $\rho_{\text{spin}}(0)$ is the electron spin density at the nucleus. $\mathbf{T}$ tensors [41] in this work are calculated using the full spin-polarized density matrix $P_{\mu\nu\sigma}$ and Bloch basis functions $\phi_{\mu\sigma}$. Spin-orbit coupling is not included in the Hamiltonian. The sum over single-electron spins σ in Eq. (5) means that the spin $\mathbf{S}$ is a spin-half operator in a quantized form of Eq. (2). When $\mathbf{A}$ is isotropic with positive diagonal elements A_0 and $\mathbf{I}$ and $\mathbf{S}$ are spin-half operators, H_{hf} has a singlet ground state and a triplet excited state lying A_0 above the ground state. In this work the magnetic degrees of freedom are treated classically, and the spin $\mathbf{S}$ is written as $\mathbf{n}S$, where $\mathbf{n}$ is a unit vector in three-dimensional space and S has a magnitude of one half.

A. NMR resonance frequency

The order of interaction strengths in the Hamiltonian in Eq. (1) in an external field of 1 T is $H_{ez} > H_{hf}(\mathbf{A}_0) > H_{hf}(\mathbf{A}_1) > H_{nz}$, with magnitudes of 50 000, 70, 10, and 1 MHz, respectively. Since the electron Zeeman term dominates, orientations of electron magnetic moments are determined mainly by the external field orientation and magnetocrystalline anisotropy (MCA). The field used in Mizoguchi's work was 1.3 T [37], which is nearly sufficient to saturate the magnetization along each of the easy, intermediate, and hard (c, b, and a) magnetization axes [12].

Hyperfine terms in the Hamiltonian can be expressed in the form of nuclear magnetic moments coupled to an effective magnetic field $\mathbf{B}_E$. Rewriting the hyperfine coupling of electron and nuclear spins [Eq. (2)] in terms of the nuclear magnetic moment $\mu_n = g_n\beta_n\mathbf{I}$ as

$$H_{hf} = -\mu_n \cdot \mathbf{B}_{hf}, \tag{6}$$

the hyperfine field can be identified from Eq. (2) as

$$\mathbf{B}_{hf} = -\frac{\mathbf{A}}{g_n\beta_n} \cdot \mathbf{n}S. \tag{7}$$

The effective field at the nucleus $\mathbf{B}_E$ is the sum of the external field and the field due to electron magnetic moments. NMR resonance frequencies and quantization axes are determined by the magnitude and direction of $\mathbf{B}_E$, respectively, at each Fe site. Electron magnetic moments are assumed to be parallel to the external field since a field of 1.3 T is sufficient to nearly saturate the magnetization along each of the crystal axes [12]. There is strong exchange coupling between Fe A and B sites, which maintains the ferrimagnetic character of magnetite. The magnetization is assumed to be parallel to Fe B-site spins in the external field. The unit vector $\mathbf{n}$ is therefore parallel (antiparallel) to the external field $\mathbf{B}_{\text{Ext}}$ for B (A) sites. In this case, it is convenient to write the small external field contribution to $\mathbf{B}_E$ as $\pm B_{\text{Ext}}\mathbf{n}$ and include it in the Hamiltonian as part of the Fermi contact term [Eq. (3)]. When both $\mathbf{A}_0$ and $\mathbf{A}_1$ are included in the hyperfine coupling matrix $\mathbf{A}$, the magnitude of the effective field is

$$B_E = \frac{S}{g_n\beta_n}\left[A_0^2 + 2A_0\mathbf{n}^T \cdot \mathbf{A}_1 \cdot \mathbf{n} + (\mathbf{A}_1 \cdot \mathbf{n})^T (\mathbf{A}_1 \cdot \mathbf{n})\right]^{1/2}, \tag{8}$$

and the resonance frequency ν (in MHz) is

$$\nu = \frac{S}{10^6 h}\mu_n \Delta M_I B_E, \tag{9}$$

where ΔM_I is the change in nuclear spin quantum number M_I and is equal to unity for a spin-half nucleus. The first term on the right-hand side of Eq. (8) is dominant, particularly for A sites where hyperfine anisotropy is small. The third term is relatively small, and the cross term between the Fermi contact term and the dipolar coupling determines variations of resonance frequencies with external magnetic field direction. Note that A_0 is positive for A sites and negative for B sites since their spin orientations are antiparallel in ferrimagnetic magnetite. The sign is determined by the sign of the electron spin density at the nucleus in Eq. (3).

B. Electron g factor

The relationship between the electron magnetic moment $\hat{\mu}_e$ and total electron angular momentum $\hat{\mathbf{J}}$ operators is

$$\hat{\mu}_e = -\beta_e \mathbf{g} \cdot \hat{\mathbf{J}}, \tag{10}$$

where $\mathbf{g}$ is the electron g tensor. In atoms, with spherical symmetry and no angular momentum quenching, the Landé g factor g_L is the appropriate g factor, and the total electron angular momentum operator is $\hat{\mathbf{J}} = \hat{\mathbf{L}} + \hat{\mathbf{S}}$. For the neutral Fe atom and the Fe^{2+} ion in their ground-state $3d^6s^2$ and $3d^6$ configurations, the $^5D_4$ states are the ground states [42], and the experimentally measured g_L value, 1.50020, is close to the theoretical value of 1.5.

Scalar g values for magnetite from ferromagnetic resonance experiments have been reported to be 2.06 [43] (below T_V), 2.20 [44], and 1.93 from gyromagnetic measurements [44]. Kittel has proposed an explanation for the different g values obtained by these two methods [44]. Sharma measured the g value in polycrystalline magnetite to be 4.06 at liquid-nitrogen temperature [45] using ferromagnetic resonance. In this work, the value of g in Eqs. (3) and (4) is adjusted to give optimum agreement with resonance frequencies measured by Mizoguchi [37]. This value is $g = 1.56$, and the same (isotropic) value is used for all A and B sites.

III. RESULTS

A. Crystal structure

The crystal structure of Cc magnetite was calculated using a hybrid density functional theory method described in detail in Ref. [38]. Calculations reported in this work used the same code [46] and basis sets as before. A variant of the Becke three-parameter Lee-Yang-Parr (B3LYP) Hamiltonian

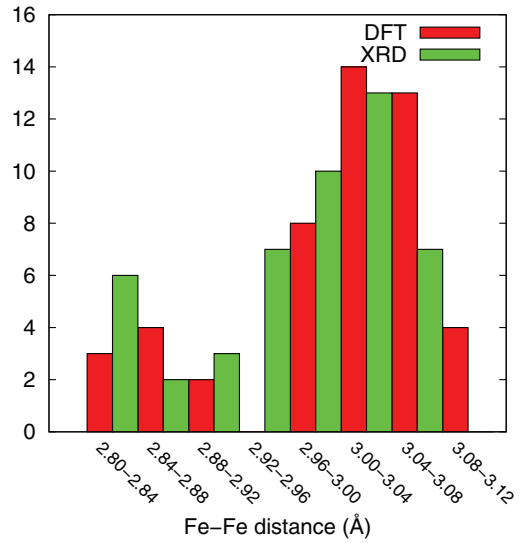

FIG. 3. (Color online) Bimodal distribution of 48 Fe-Fe distances in Cc magnetite from XRD [17] and DFT calculation.

TABLE I. Short Fe-Fe distances from DFT total energy minimization and XRD (in Å) and minority-spin charge populations on B-site ions (in units of e).

	Charge (units of e)			Bond length (Å)	
Fe pair	Left	Right	Sum[a]	DFT	XRD[b]
B33-B1a1	0.45	0.63	1.08	2.818	2.820
B33-B1b1	0.45	0.65	1.09	2.881	2.832
B33-B44	0.45	0.64	1.09	2.858	2.838
B32-B41	0.45	0.60	1.05	2.836	2.813
B32-B1a2	0.45	0.61	1.06	2.973	2.853
B32-B1b1	0.45	0.65	1.10	2.877	2.848
B31-B1b2	0.44	0.48	0.92	2.834	2.820
B42-B2a2	0.52	0.39	0.91	2.839	2.837
B34-B1a2	0.26	0.61	0.87	2.864	2.914
B2b1-B2a1	0.53	0.29	0.82	2.884	2.913

[a]Mulliken populations on Fe B sites sum to 14.2e out of 16.0e. The remaining electrons in these bands are delocalized over O and Fe A sites.
[b]Reference [17].

[47] was used in which the weight of Fock exchange was reduced. Inclusion of Fock exchange in the DFT Hamiltonian increases the band gap of a semiconducting oxide, compared to, for example, a generalized gradient approximation (GGA) DFT Hamiltonian. Our previous work [38] found that a GGA Hamiltonian predicts the high-temperature phase of magnetite with $Fd\bar{3}m$ space-group symmetry to be the ground state, whereas hybrid DFT [38] and DFT + U [20,21,23] approaches predict symmetry-broken structures typical of magnetite below T_V.

The structure from the recent x-ray refinement on a monodomain microcrystal [17] was used as the starting geometry for structure relaxation. Lattice parameters and the monoclinic angle found by total energy minimization were 12.022, 11.966, and 16.975 Å and 90.209°, and these values may be compared with values of 11.888, 11.849, and 16.775 Å and 90.236° from XRD [17]. Distributions of Fe-Fe bond lengths from XRD and this work are compared in Fig. 3. Lengths of short bonds and Mulliken populations of 16 minority-spin 3d electrons which occupy 16 bands just below the valence-band maximum are given in Table I. XRD [17] finds eight short Fe-Fe distances less than 2.86 Å, while DFT total energy minimization predicts nine short Fe-Fe distances less than 2.89 Å. The median Fe-Fe distance lies in the range 3.00 to 3.04 Å. These values mark the boundaries between the two parts of the bimodal distribution of Fe-Fe distances shown in Fig. 3. The difference in thresholds is expected as hybrid DFT lattice relaxation overestimates experimental lattice constants by around 1% (0.03 Å).

The main differences in short Fe-Fe bond lengths from XRD and hybrid DFT are the B33-B1b1, B32-B1a2, and B34-B1a2 bond lengths. Other bond lengths agree to within 0.03 Å, while these distances differ by 0.05, 0.12, and 0.05 Å, respectively. Each of these bonds involves one of the capping ions in the zigzag chain. Since these atoms are connected via delocalized, asymmetric one-electron bonds, charge may transfer relatively easily from one ion to its neighbor, leading to lengthening or shortening of particular bonds. Six of the eight Fe-Fe distances in each zigzag chain are short (B34-B1a2, B1a2-B32, B32-B1b1, B1b1-B33, B33-B1a1, B31-B1b2), excluding branching ions B41 and B44. Distances to the B32 ion are elongated in DFT relaxation compared to XRD (+0.12 ÅB32-B1a2 and +0.03 ÅB32-B1b1), while the B34-B1a2 distance is contracted by 0.05 Å. The reason for these differences is not clear. It could be a result of an experimental error in the B32 position, strong coupling of charge distribution and bond lengths in asymmetric one-electron bonds, etc. Differences in atomic positions and charge distribution on relaxing the structure away from the XRD structure in a DFT calculation might be expected to produce corresponding changes in predicted NMR frequencies. Supplemental Table III shows that the largest changes in predicted frequency (with the external magnetic field aligned with the crystal c axis) occur at sites B44 (+3.1 MHz), B32 (−2.1 MHz), and B2a1 (−3.6 MHz). All other sites have predicted frequency changes of less than 2 MHz on structure relaxation.

As noted above, Fe B-site ions in magnetite occupy a quasitetrahedral lattice (Fig. 1). The Cc magnetite structure can be regarded as one with four unique rows of B-site ions, each with a period of four B-site ions, where each row is parallel to either the a or b conventional unit-cell axis. The naming convention for B-site ions introduced by Senn and coworkers [17] is used here. The four unique rows of B-site ions at different fractional heights in the unit cell z are the B1 row ($z = 4/8$), the B2 row ($z = 6/8$), and two mixed B3/B4 rows at $z = 5/8$ and $7/8$. The B1 and B2 rows are parallel to the a axis, and the B3/B4 rows are parallel to the b axis. Structures of each of the eight unique Fe_4 tetrahedra in Cc magnetite and their orbital orders are given in the Supplemental Material.

There is one element of symmetry in the Cc space group, a glide plane parallel to the ac plane with a translation of $0.5c$. B1 row ions lie very close to the glide plane, referred to by Mizoguchi [37] as a "pseudomirror plane" in his assignment of NMR resonances to particular B sites. Orbital order on the B sites is described in terms of the usual labels for sites with perfect octahedral symmetry. In the present case,

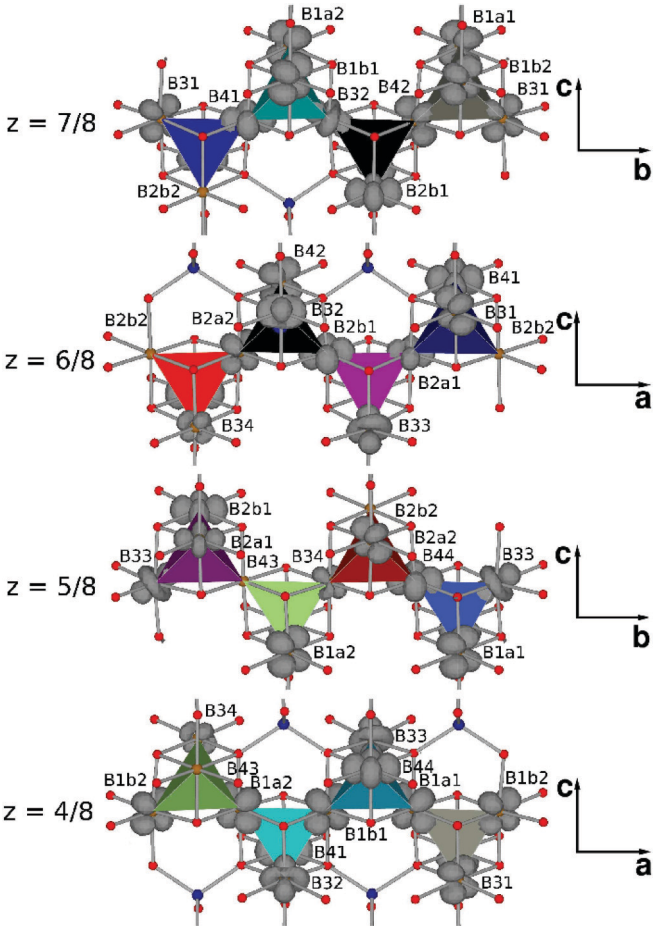

FIG. 4. (Color online) Charge-density isosurface derived from 16 occupied minority-spin bands just below the Fermi level viewed along the B1, B2, and B3/B4 rows of Fe B-site ions. Unique Fe B-site tetrahedra are shown in different colors.

the Cartesian axes used to evaluate hyperfine anisotropy **T** tensors are (nearly) parallel to the a, b, and c directions of the conventional Cc unit cell. FeO_6 octahedra are rotated by 45° about the c axis with respect to these axes, so that designations of orbitals as $3d_{xy}$ and so on function only as labels. Mulliken populations range from 0.07e (B2b2 and B43 sites, not given in Table I) to 0.65e (B1b1 and B44). However, *total* charge and spin populations for B-site ions have a much smaller range than minority spins in this group of bands (see Supplemental Material).

B. Charge and orbital order

Charge and orbital order in magnetite arises mainly from the 16 minority-spin electrons localized on Fe B sites. They occupy a narrow, almost dispersionless group of states just below the Fermi level (see Supplemental Material). Figure 4 shows a charge-density isosurface for these electrons. They form eight one-electron bonds between neighboring Fe B-site ions, and eight electrons are delocalized in a broken zigzag chain. One-electron bonds consist of 3d orbital configurations on neighboring Fe sites in which t_{2g} orbitals are directed towards each other and have a total charge population close to one electronic charge, 1.0e ± 0.1e. One-electron bonds are found between sites B31-B1b2, B42-B2a2, B34-B1a2, and B2a1-B2b1 (Fig. 4). Electrons delocalized on the zigzag chain are found on sites B1a2, B32, B1b1, B33, and B1a1 and the chain branches at B32 and B33 to include B41 and B44 sites. Zigzag chain B-site pairs which include B32 or B33 sites (B32-B41, B32-B1a2, B32-B1b1, B33-B1a1, B33-B1b1, and B33-B44) have ion-pair charge populations in the range 1.05e to 1.09e.

The zigzag chain in Cc magnetite highlighted in this work is obviously related to the "trimerons" postulated by Senn and coworkers [17,23]. However, there are some significant differences in the interpretation of the structure and minority-spin charge distribution from DFT calculations in Refs. [17,23] and this work. The trimeron concept is one where an Fe minority-spin electron on a (formally) Fe^{2+} ion delocalizes onto two neighboring (formally) Fe^{3+} ions, so that one electron is delocalized over three sites. In this work it is shown that minority-spin electrons are shared between Fe ions as discrete one-electron bonds or in larger zigzag chain structures, which branch to include B41 and B44 site ions.

Inspection of Fig. 4 shows that all orbitals except those on the B2b2, B32, B33, and B43 sites are t_{2g} orbitals. Orbitals in the B1 row at $z = 4/8$ are either d_{xz} or d_{yz} and alternate along the row. Orbitals on B sites in the layer below are either d_{xz} (B31), d_{yz} (B42), or d_{xy} (B41). Relative orientations of orbitals in adjacent layers can be aligned (d_{xz}-d_{xz} or d_{yz}-d_{yz}), perpendicular (d_{xz}-d_{yz}, d_{xy}-d_{xz}, or d_{xy}-d_{yz}), or parallel (d_{xy}-d_{xy}). Pairs B1b2-B31, B1a1-B31, and B2a1-B41 are examples of each kind. Within rows, orbitals may be perpendicular (d_{xz}-d_{yz}) or aligned (d_{xy}-d_{xy}). Pairs B1a1-B1b1 and B2a1-B2b1 are examples of these kinds of relative orbital orientations. When pairs of orbitals in adjacent rows or the same row are aligned, a short Fe-Fe bond exists, and the bond on the opposite side of the tetrahedron is the longest in the tetrahedron in all but one case (see Supplemental Material). Charge density in the minority-spin bands below the Fermi level is nearly zero on the B2b2 and B43 sites. They will be referred to as Fe^{3+} sites.

B32 and B33 ions are distinct in that they have "d_{z^2}" charge densities which are directed along axes containing adjoining tetrahedra. This hybridization on the B32 and B33 sites is also seen in Fig. 3 of Ref. [23]. They are part of a zigzag chain (B1a2, B32, B1b1, B33, B1a1) where short bonds are formed. Short bonds are also formed between B32-B41 and B33-B44 pairs. Ions at the apexes of this chain (B32 and B33) have a low charge (0.45e; Table I), and those in the center have higher charges (over 0.6e). Senn and coworkers described the charge order in this chain as trimerons in which Fe^{2+} ions share minority-spin 3d electrons with two neighboring Fe^{3+} sites [17,23]. One-electron bonds between ions in the two tetrahedra which contain the zigzag chain have a population greater than 1.0e. Discrete one-electron bonds exist between B31-B1b2, B42-B2a2, B34-B1a2, and B2b1-B2a1 pairs, and the electron count is less than unity in these bonds (Table I).

The atom-projected densities of states (DOS) for 14 of the 16 Fe B sites are shown in Fig. 5. B sites which exist as Fe^{3+} have almost no minority-spin DOS in this energy range and are not shown. Each of the top four panels shows the projected DOS for pairs of B sites connected by discrete one-electron

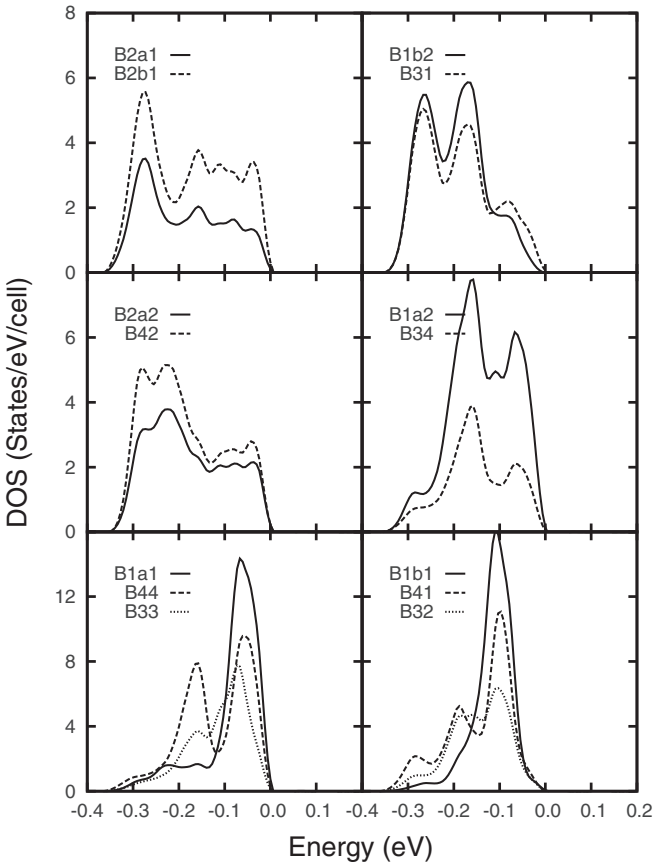

FIG. 5. Atom-projected densities of states for B sites in Cc magnetite. DOS are grouped as pairs of ions which form one-electron bonds or parts of the zigzag chain along the B1 row.

bonds. For each of these cases, the DOS for each site are similar, as might be expected for single electrons shared by those site pairs. The bottom two panels show DOS for the six sites in zigzag chains. The DOS for each site shows three peaks close to the Fermi level.

C. Fermi contact hyperfine field

The largest contribution to the hyperfine field at the nucleus [Eq. (7)] is the Fermi contact part [Eq. (3)]. It is notoriously difficult to calculate accurately as values obtained depend markedly on basis sets used and there are contributions of either sign to the spin density at the nucleus $\rho_{\rm spin}(0)$ from successive ns shells. Magnetic susceptibilities were calculated for Fe^{2+} and Fe^{3+} ions and are compared to previous work.

Early calculations of Fermi contact hyperfine fields in Fe ions were carried out by Bagus and coworkers [48,49] and Freeman and Watson [50,51] using unrestricted Hartree-Fock (UHF) wave functions. These authors reported values of the static magnetic susceptibility,

$$\chi = \frac{4\pi}{N_S}\rho_{\rm spin}(0), \tag{11}$$

where N_S is the number of unpaired spins [51]. Table II gives a comparison of static magnetic susceptibilities from this earlier work to values from UHF and hybrid DFT calculations, which used the same basis set as calculations for magnetite.

TABLE II. Magnetic susceptibilities from UHF and hybrid DFT Hamiltonians for Fe ions (in atomic units).

Species	Fe^{2+}	Fe^{3+}
UHF[a]	−3.29	−3.00
UHF[b]	−3.872	
UHF[c]	−3.763	−3.503
Hybrid DFT[c]	−2.372	−2.377

[a]Reference [51].
[b]Reference [49].
[c]This work.

A nonzero spin density at the nucleus of the Fe atom arises because of an uncompensated exchange interaction between electrons in the Fe $3d$ shell and electrons in $1s$, $2s$, $3s$, and $4s$ shells. A negative sign implies that the spin density at the nucleus has a sign opposite to that of the spin density of the polarizing $3d$ shell. Calculations by Watson and Freeman [51] for the Fe atom showed that the largest contribution comes from the $2s$ shell (−7.72) and that this is largely canceled by contributions from the $3s$ and $4s$ shells (+4.31, +2.92). The tightly contracted $1s$ shell has little overlap with the $3d$ wave functions and contributes −0.10. Atomic beam magnetic resonance measurements found agreement between measured [52] and calculated [48] values of the isotropic hyperfine coupling constant for the ^5D_J states of the Fe atom for $J = 1$ to 4.

Contractions of Gaussian orbital primitives in the Fe basis set (see the Appendix) were relaxed in this work to allow adequate flexibility in describing spin polarization in inner s shells. Susceptibility values from UHF wave functions for Fe^{2+} and Fe^{3+} ions in Table II are in reasonable agreement with literature values. There is a marked difference in susceptibility values obtained using hybrid DFT and UHF spin densities. Recent calculations have shown that a hybrid DFT approach to calculating Fermi contact parameters in a number of small molecules containing transition and main group elements [53–55] yields improved agreement with experiment or coupled-cluster calculations.

D. NMR resonance frequencies in magnetite

NMR resonance frequencies for A and B sites, which include both $\mathbf{A}_0$ and $\mathbf{A}_1$ terms in the hyperfine field, are presented in Figs. 6–9 as a function of external field direction and are compared to frequencies from Ref. [37]. A single parameter, a scalar value for the electron g factor, discussed in Sec. II B, was adjusted to fit all A- and B-site frequencies in Figs. 6–9. It was chosen to give the best agreement with A-site resonance frequencies. Numerical values of resonance frequencies with the magnetic field aligned with the c axis are given in the Supplemental Material.

In Cc magnetite, the glide plane parallel to the ac plane in the conventional unit cell generates equivalent pairs of Fe ions for both A and B sites. Under this symmetry operation, diagonal and xz entries in the $\mathbf{T}$ tensor are even, and the xy and yz entries are odd. These symmetry properties determine the number of predicted frequencies for a particular Fe site and external field direction. For example, when the external

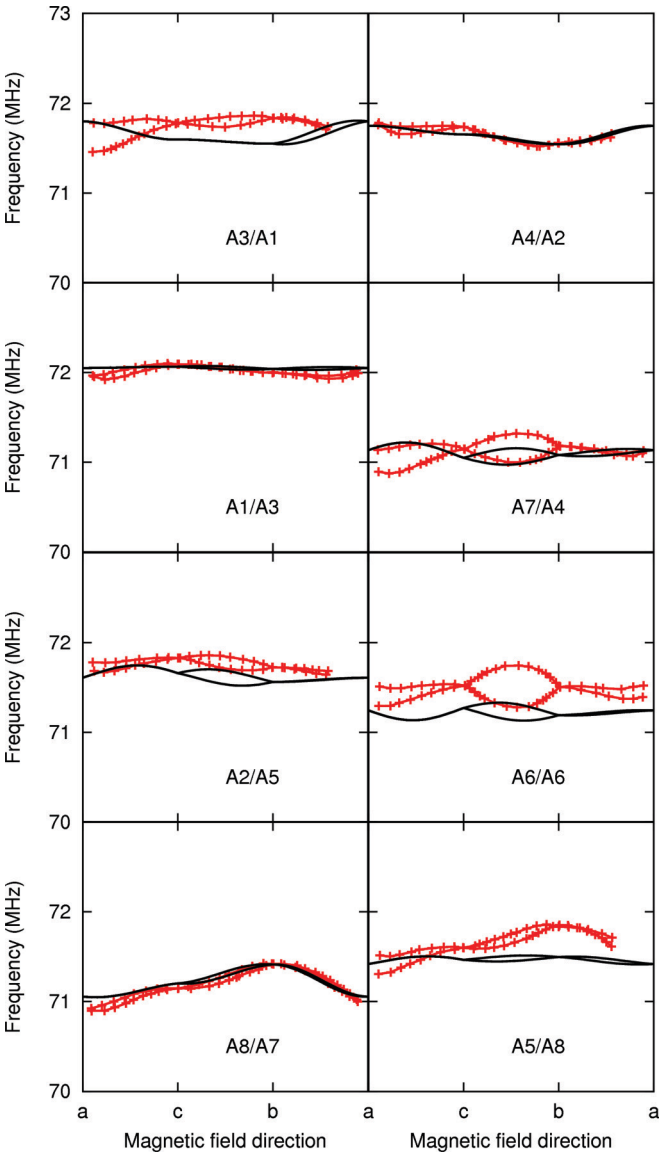

FIG. 6. (Color online) NMR resonance frequencies of Fe A sites from experiment [37] (crosses) and theory (solid curves). A-site labels from Refs. [37] (left) and [17] (right) are used.

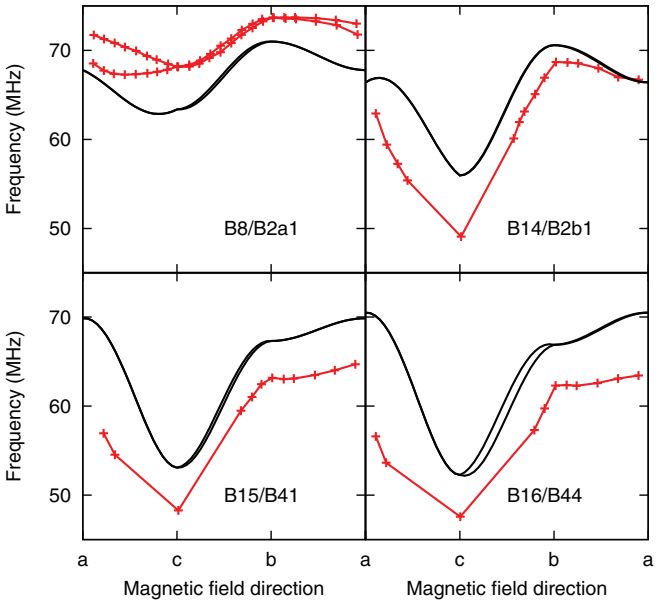

FIG. 7. (Color online) NMR resonance frequencies of Fe B sites from experiment [37] (crosses) and theory (solid curves) with $3d_{xy}$ orbital order. B-site labels from Refs. [37] (left) and [17] (right) are used.

field lies in the ac plane, xx, xz, and zz entries in the **T** tensor determine resonance frequencies, according to Eq. (8). (By assumption, A- and B-site electron magnetic moments are antiparallel and parallel to the external field, respectively). By symmetry, ion pairs which are related by the glide-plane symmetry operation have the same sign for these elements. Hence a single degenerate frequency is predicted when the external field is in the ac plane in Figs. 6–9. On the other hand, when the field is in the bc plane, the yy, yz, and zz entries determine the resonance frequencies. yz tensor entries for ions related by the glide-plane symmetry operation have opposite signs, and two nondegenerate frequencies are predicted for each symmetry-related Fe ion pair.

Labels for sites (shown in Fig. 4) assigned to particular resonances are given in Figs. 6–9 together with labels used by Mizoguchi for particular NMR resonances. Data in Figs. 6–9 are grouped according to the characteristic variation of NMR resonance frequency with external field direction. They therefore show the number of sites with specific types of orbital order. Figure 6 shows resonance frequencies for all A sites, where there is no expected charge order and little variation of frequency with applied field direction. Figure 7 shows four B sites with $3d_{xy}$ orbital order (by inspection of the charge density shown in Fig. 4), Fig. 8 shows six B sites with $3d_{xz}$ or $3d_{yz}$ orbital order, and Fig. 9 shows one further site with $3d_{xz}$ or $3d_{yz}$ orbital order, two sites with $3d_{z^2}$ orbital order, and two with essentially Fe^{3+} character and little orbital order. Data for the B14, B15, and B16 sites in Fig. 7 have been redrawn from Ref. [37] as single lines (and not split lines) since splitting is small and Mizoguchi's data for these sites are sparse. Curves for these sites calculated using Eqs. (8) and (9) show very little splitting.

Reasonable fits to experimental curves in Fig. 6 can be found for most of the eight unique A sites. Weak dependence on the external field direction is found for A4/A2 and A1/A3 sites. Frequencies for particular sites split when the external field is in the bc plane for ions assigned to the A1, A4, A5, A6, and A8 sites. These splittings occur because yz elements of **T** tensors for these sites differ in sign for pairs of A-site ions which are symmetry related by the glide plane. Splittings also occur in experimental data when the external field is in the ac plane for ions assigned to the A1, A4, A6, and A8 sites. This splitting is not predicted in our calculations. This is discussed further below and is attributed to twinning [37]. The predicted degree of splitting is less than is observed in experiment for A4 and A6 sites, and there is no apparent fit for the line labeled A3 by Mizoguchi. It should be noted that the degree of hyperfine anisotropy is very small for A sites and that the frequency variation with external field direction is always less than 1 MHz, as expected for nearly spherically symmetric Fe^{3+} ions.

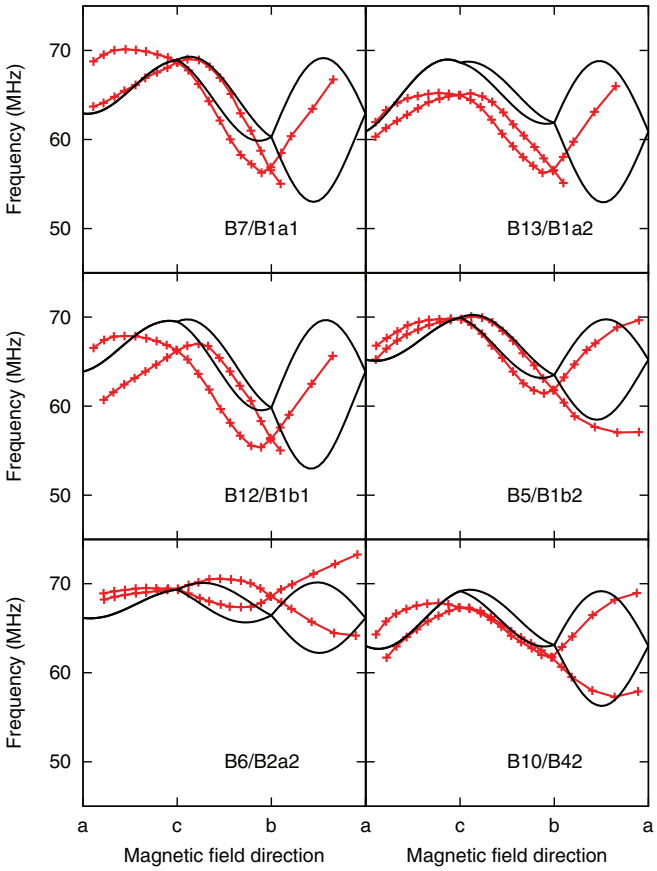

FIG. 8. (Color online) NMR resonance frequencies of Fe B sites from experiment [37] (crosses) and theory (solid curves) with $3d_{xz}$ and $3d_{yz}$ orbital order. B-site labels from Refs. [37] (left) and [17] (right) are used.

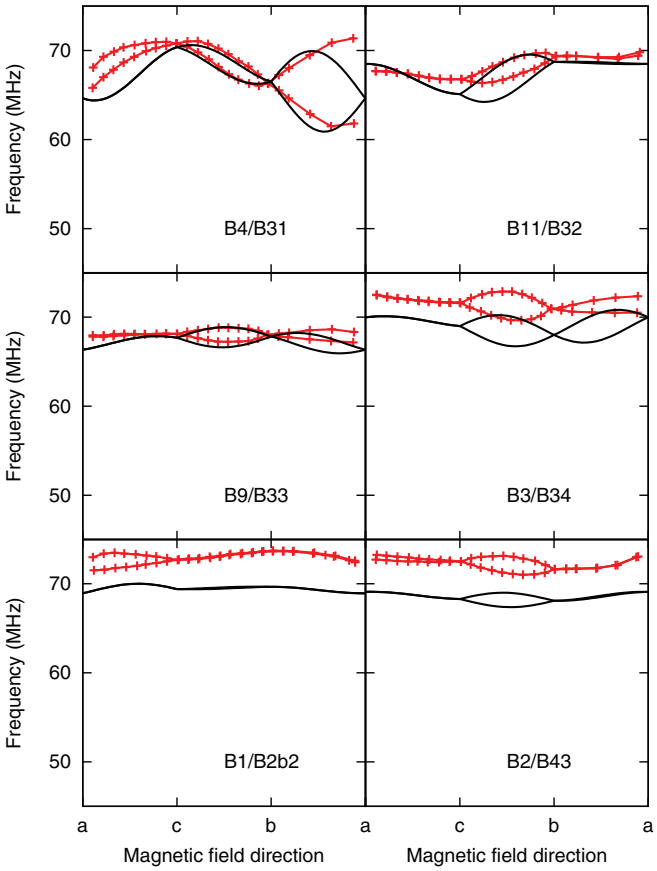

FIG. 9. (Color online) NMR resonance frequencies of Fe B sites from experiment [37] (crosses) and theory (solid curves) with $3d_{z^2}$ orbital order or an Fe^{3+} configuration. B-site labels from Refs. [37] (left) and [17] (right) are used.

Resonances in Fig. 7 are assigned to B sites with $3d_{xy}$ orbital order. They show strong dips in frequency when the external field is aligned with the c axis. In that case, the zz entry of the $\mathbf{A}_1$ tensor determines the anisotropic hyperfine shift. Similarly, when the field is aligned with the a or b axes, xx or yy entries of the tensor determine the shift. $\mathbf{A}_1$ tensors for these sites have large positive zz entries and nearly equal xx and yy negative entries. Since A_0 is negative for B sites, Eqs. (8) and (9) predict a reduction in resonance frequency when the external field is aligned with the c axis. The upper panels in Fig. 7 show predicted frequencies for the B2a1 and B2b1 sites and compare them to measured frequencies from sites denoted B8 and B14 in Ref. [37]. The B2a1 and B2b1 sites share one electron in a one-electron bond (see Fig. 4). The B2b1 site has the largest fraction of the charge (0.53e; Table I) compared to the B2a1 site (0.29e), and consequently, the B2b1 site has the largest dip in frequency when the external field is aligned with the c axis. The B41 and B44 sites are assigned to Mizoguchi's B15 and B16 resonances. These sites have large fractions of an orbital ordered $3d_{xy}$ electron (0.60e and 0.64e, respectively; Table I) and, consequently, large diagonal elements of the $\mathbf{A}_1$ tensor and large frequency dips when the external field is along the c axis.

Resonances in Fig. 8 are attributed to B sites with $3d_{xz}$ and $3d_{yz}$ orbital order. Experimental curves show similar shapes: splitting when the external field is in the ac plane, splitting and a downwards shift in frequency as the field moves from the c axis to the b axis in the bc plane, and a large splitting with the field in the ab plane. The latter splitting is predicted to go to zero as the field becomes aligned with the a axis; however, it does not go to zero for any of these sites. This may be because the magnetization is not saturated when the external field is along the hard a axis. This point is discussed further in the next section. The B1a1, B1a2, B1b1, and B1b2 sites in the zigzag chain and the B2a2 and B42 sites in a one-electron bond (see Fig. 4) are assigned to sites labeled B7, B13, B12, B5, B6, and B10 by Mizoguchi. All of these sites have $3d_{xz}$ or $3d_{yz}$ orbital order and, consequently, similar variations of frequency with external magnetic field direction.

The resonance at the site labeled B4 by Mizoguchi, shown in Fig. 9, has a frequency dependence on external magnetic field direction similar to other assigned sites with $3d_{xz}$ or $3d_{yz}$ orbital order. It is assigned to site B31, which forms a one-electron bond with site B1b2 (Fig. 4). The remaining B sites in Fig. 9 are assigned to Fe ions at the apexes of zigzag chains (B11/B32, B9/B33, and B3/B34) and the two B-site ions with an Fe^{3+} configuration (B1/B2b2 and B2/B43). In each case there is good agreement between theory and experiment for the variations of resonances with external field direction. In three cases (B1/B2b2, B2/B43, and B3/B34) the computed frequency lies below the measured frequency by about 5 MHz.

IV. DISCUSSION AND CONCLUSIONS

In this section the insight provided by hybrid DFT calculations into the electronic configurations of Fe A- and B-site ions and the charge and orbital order associated with minority-spin $3d$ electrons in 16 bands just below the Fermi level is used to gain further understanding of the variation in NMR frequencies with external field direction. Possible reasons for the fact that measured NMR resonances do not become degenerate for specific Fe ions when the external field is along the a axis and why resonances split when the external field is in the ac plane are also discussed.

Degeneracy of predicted pairs of resonances with the field aligned with the a axis is not found in the experimental data but is predicted by Eqs. (8) and (9). This is likely to be because the a axis is the magnetically hard axis and a field of 1.3 T may not be sufficient to fully polarize the crystal when the field is in this direction. Magnetization curves obtained at 10 K in Ref. [12] show that the magnetization saturates along the a axis in fields greater than 1.5 T. If experimental data shown in Figs. 6–9 were available for a significantly higher external field, say 5 T, so that degeneracies were achieved when the field is along each conventional unit-cell axis, then it would be possible to make a quantitative fit for the $\mathbf{A}_1$ tensor for a more direct comparison to data from DFT calculations. Further resolution of the resonances assigned to B sites with $3d_{xy}$ orbital order with the field along the c axis (Fig. 7) is also desirable.

The observation of a pair of lines when the field is in the ac plane may be caused by the existence of more than one microdomain below T_V, or it may be due to magnetization lying slightly outside the ac plane. Eight distinct microdomains are generated by application of the identity operation and xy, xz, and yz mirror-plane operations to the conventional lattice vectors. These elements are not present in the Cc space group, but since the monoclinic angle (90.236°) is very close to 90°, these domains may coexist at little energy cost. Operations in which new a or b axes are generated do not generate additional resonance lines along bc or ab directions, but an inverted c axis will generate an additional xz element in the $\mathbf{T}$ tensor with the opposite sign. Hence observation of pairs of resonances with the field in the ac direction may be caused by the coexistence of microdomains, as noted by Mizoguchi [37]. Alternatively, since the a axis is the hard magnetic axis, the magnetic moment may cant slightly out of the ac plane when the field is in the plane. Even a small canting, of the order of 5%, can cause a splitting of lines comparable in magnitude to that seen in experiment. However, for the B sites assigned to $3d_{xz}$ and $3d_{yz}$ orbital order, the curvature is opposite to that seen in experiment. Hence the more likely cause of pairs of resonances when the field is in the ac plane is the existence of microdomains.

In summary, Fermi contact and magnetic dipolar contributions to the hyperfine fields at nuclei of the charge and orbital ordered state of magnetite which exists below the Verwey temperature have been calculated using a hybrid DFT method. The crystal structure used for calculations was refined in the experimentally observed Cc space group [17]. The charge and orbital order which is found for this structure can be described in terms of one-electron bonds formed by minority-spin $3d$ electrons on octahedral Fe B sites and by branched zigzag chains of one-electrons bonds, or trimerons [17,23]. Calculations of orbital order on Fe B sites show that 4 out of 16 unique B sites have $3d_{xy}$ orbital order, 7 have $3d_{xz}$ or $3d_{yz}$ orbital order, 3 (which cap zigzag chains) have $3d_{z^2}$ orbital order, and 2 are essentially Fe^{3+} ($3d^5$). NMR resonance frequencies for each unique A and B site in magnetite, measured as a function of external field direction for a spherical single crystal at 4.2 K [37], can be fitted to predicted resonance frequencies for this charge and orbital ordered state using Fermi contact and magnetic dipolar contributions to hyperfine fields at ^{57}Fe nuclei. Further experimental measurements with a stronger external magnetic field are desirable to allow a quantitative fit to the computed tensor which couples nuclear and electron spins in magnetite.

Cc magnetite bears some resemblance to the M_1 gapped phase of VO_2 where the character of the metal-insulator transition in VO_2 has been described as a Peierls-Mott transition [32,34,35]. In that case both dimerization of d^1 V sites and strong Coulomb correlations contribute to the transition at 342 K. The structure transforms from a tetragonal conducting state with the rutile structure denoted R to a monoclinic $P2_1/c$ M_1 structure. V-V distances change from 2.87 to 2.65 and 3.12 Å in the dimerized state. Dimerization occurs via d_σ symmetry orbitals oriented along the rutile-structure c axis, which form a partly filled metallic band in the R phase and split in the insulating M_1 phase. The situation in magnetite is different in that there is one minority spin per pair of Fe B sites rather than one per site. Instead of forming covalent dimer singlets, one-electron bonds generate a narrow band, with a bandwidth of 0.3 eV.

ACKNOWLEDGMENTS

The author is grateful to J. P. Attfield for helpful discussions. Calculations were performed on the Kelvin and Stokes clusters maintained by the Trinity Centre for High Performance Computing and the Irish Centre for High End Computing. The Kelvin cluster was funded through grants from the Irish Higher Education Authority PRTLI program. The project was supported by Science Foundation Ireland under Grant No. 09/RFP/MTR/2295.

APPENDIX A: DETAILS OF CALCULATIONS

Calculations reported in this work used the CRYSTAL09 code [46]. All electron Gaussian orbital basis sets used were an Fe $20s14p5d$ basis contracted to $7s6p2d$, previously used to study hematite [56] (with a different contraction), and an O $14s6p1d$ basis contracted to $5s4p1d$, previously used to study NiO [57], where the d polarization function had an exponent of 0.5. The effect of uncontracting various shells of Gaussians in the Fe basis set on values of the spin density at the nucleus (and $\mathbf{A}_0$ parameters) was investigated using Fe^{2+} and Fe^{3+} ions in free space. Two contracted shells of Gaussian sp orbitals in the Fe basis set were partly uncontracted. This adjustment to the Fe basis set was found to be important in obtaining converged values for A_0 parameters. Total energy calculations were performed using a $6 \times 6 \times 6$ Monkhorst-Pack net [58]

for the Cc unit cell and a $12 \times 12 \times 12$ net for the $Fd\bar{3}m$ unit cell.

A variant of the B3LYP Hamiltonian [47] was used in which the weight of the Fock exchange was reduced below the standard value of 20%. Inclusion of the Fock exchange in the DFT Hamiltonian increases the band gap of an oxide, compared to, for example, a GGA DFT Hamiltonian. Our previous work [38] found that a GGA Hamiltonian predicts the high-temperature phase of magnetite with $Fd\bar{3}m$ space-group symmetry, whereas hybrid DFT [38] and DFT + U [20,21,23] approaches predict symmetry-broken structures typical of magnetite below T_V. The B3LYP hybrid density functional [59,60] contains Hartree-Fock exchange with weight A; the local-density approximation to exchange E_x^{LDA} [61] with weight $(1 - A)$; Becke's gradient-corrected exchange functional E_x^{Becke} [47] with weight B; the Lee, Yang, and Parr approximation to the correlation functional E_c^{LYP} [62] with weight C; and the Vosko, Wilks, and Nusair approximation to the electron correlation functional E_c^{VWN} [63] with weight $(1 - C)$,

$$E_{xc} = (1 - A)\left(E_x^{\mathrm{LDA}} + B E_x^{\mathrm{Becke}}\right) + A E_x^{\mathrm{HF}} + (1 - C) E_c^{\mathrm{VWN}} + C E_c^{\mathrm{LYP}}. \quad \text{(A1)}$$

The weights of Fock exchange, A, tested in this work were 5%, 10%, and 15%. At 5%, a metallic state is predicted for Cc magnetite, and at the higher weights, band gaps of 0.5 and 0.9 eV are predicted. The results given in this work are all for 10% Fock exchange.

[1] E. J. W. Verwey, Nature (London) **144**, 327 (1939).
[2] R. J. Goff, J. P. Wright, J. P. Attfield, and P. G. Radaelli, J. Phys. Condens. Matt. **17**, 7633 (2005).
[3] E. Nazarenko, J. E. Lorenzo, Y. Joly, J. L. Hodeau, D. Mannix, and C. Marin, Phys. Rev. Lett. **97**, 056403 (2006).
[4] D. J. Huang, H.-J. Lin, J. Okamoto, K. S. Chao, H.-T. Jeng, G. Y. Guo, C.-H. Hsu, C.-M. Huang, D. C. Ling, W. B. Wu *et al.*, Phys. Rev. Lett. **96**, 096401 (2006).
[5] J. Schlappa, C. Schler-Langeheine, C. F. Chang, H. Ott, A. Tanaka, Z. Hu, M. W. Haverkort, E. Schierle, E. Weschke, G. Kaindl *et al.*, Phys. Rev. Lett. **100**, 026406 (2008).
[6] J. E. Lorenzo, C. Mazzoli, N. Jaouen, C. Detlefs, D. Mannix, S. Grenier, Y. Joly, and C. Marin, Phys. Rev. Lett. **101**, 226401 (2008).
[7] J. García, G. Subías, J. Herrero-Martín, J. Blasco, V. Cuartero, M. C. Sánchez, C. Mazzoli, and F. Yakhou, Phys. Rev. Lett. **102**, 176405 (2009).
[8] S. B. Wilkins, S. DiMatteo, T. A. W. Beale, Y. Joly, C. Mazzoli, P. D. Hatton, P. Bencok, F. Yakhou, and V. A. M. Brabers, Phys. Rev. B **79**, 201102 (2009).
[9] A. Tanaka, C. F. Chang, M. Buchholz, C. Trabant, E. Schierle, J. Schlappa, D. Schmitz, H. Ott, P. Metcalf, L. H. Tjeng *et al.*, Phys. Rev. Lett. **108**, 227203 (2012).
[10] L. V. Gasparov, D. B. Tanner, D. B. Romero, H. Berger, G. Margaritondo, and L. Forró, Phys. Rev. B **62**, 7939 (2000).
[11] M. P. Pasternak, W. Xu, G. Rozenberg, R. Taylor, and R. Jeanloz, J. Magn. Magn. Mater. **265**, L107 (2003).
[12] Ö. Özdemir and D. J. Dunlop, Earth Planet. Sci. Lett. **165**, 229 (1999).
[13] D. J. Huang, C. F. Chang, H.-T. Jeng, G. Y. Guo, H.-J. Lin, W. B. Wu, H. C. Ku, A. Fujimori, Y. Takahashi, and C. T. Chen, Phys. Rev. Lett. **93**, 077204 (2004).
[14] J. A. Duffy, J. W. Taylor, S. B. Dugdale, C. Shenton-Taylor, M. W. Butchers, S. R. Giblin, M. J. Cooper, Y. Sakurai, and M. Itou, Phys. Rev. B **81**, 134424 (2010).
[15] J. P. Wright, J. P. Attfield, and P. G. Radaelli, Phys. Rev. B **66**, 214422 (2002).
[16] J. Blasco, J. García, and G. Subías, Phys. Rev. B **83**, 104105 (2011).
[17] M. S. Senn, J. P. Wright, and J. P. Attfield, Nature (London) **481**, 173 (2012).
[18] G. K. H. Madsen and P. Novak, Europhys. Lett. **69**, 777 (2005).
[19] I. Leonov, A. N. Yaresko, V. N. Antonov, and V. I. Anisimov, Phys. Rev. B **74**, 165117 (2006).
[20] H.-T. Jeng, G. Y. Guo, and D. J. Huang, Phys. Rev. B **74**, 195115 (2006).
[21] K. Yamauchi, T. Fukushima, and S. Picozzi, Phys. Rev. B **79**, 212404 (2009).
[22] K. Yamauchi and S. Picozzi, Phys. Rev. B **85**, 085131 (2012).
[23] M. S. Senn, I. Loa, J. P. Wright, and J. P. Attfield, Phys. Rev. B **85**, 125119 (2012).
[24] E. J. W. Verwey and P. W. Haayman, Physica **9**, 979 (1941).
[25] L. Pauling, J. Am. Chem. Soc. **53**, 3225 (1931).
[26] D. M. Bishop, J. Chem. Phys. **53**, 1541 (1970).
[27] A. Bosak, D. Chernyshov, M. Hoesch, P. Piekarz, M. Le Tacon, M. Krisch, A. Kozłowski, A. M. Oleś, and K. Parlinski, Phys. Rev. X **4**, 011040 (2014).
[28] S. M. Shapiro, M. Iizumi, and G. Shirane, Phys. Rev. B **14**, 200 (1976).
[29] Y. Yamada, N. Wakabayashi, and R. M. Nicklow, Phys. Rev. B **21**, 4642 (1980).
[30] J. B. Goodenough, J. Solid State Chem. **3**, 490 (1971).
[31] V. Eyert, Ann. Phys. (Berlin, Ger.) **11**, 650 (2002).
[32] S. Biermann, A. Poteryaev, A. I. Lichtenstein, and A. Georges, Phys. Rev. Lett. **94**, 026404 (2005).
[33] M. Haverkort, Z. Hu, A. Tanaka, W. Reichelt, S. Streltsov, M. A. Korotin, V. I. Anisimov, H. H. Hsieh, H.-J. Lin, C. T. Chen *et al.*, Phys. Rev. Lett. **95**, 196404 (2005).
[34] T. C. Koethe, Z. Hu, M. W. Haverkort, C. Schüßler-Langeheine, F. Venturini, N. B. Brookes, O. Tjernberg, W. Reichelt, H. H. Hsieh, H.-J. Lin *et al.*, Phys. Rev. Lett. **97**, 116402 (2006).
[35] C. Weber, D. D. ORegan, N. D. M. Hine, M. C. Payne, G. Kotliar, and P. B. Littlewood, Phys. Rev. Lett. **108**, 256402 (2012).
[36] P. Novák, H.Štěpánková, J. Englich, J. Kohout, and V. A. M. Brabers, Phys. Rev. B **61**, 1256 (2000).
[37] M. Mizoguchi, J. Phys. Soc. Jpn. **70**, 2333 (2001).
[38] A. D. Rowan, C. H. Patterson, and L. V. Gasparov, Phys. Rev. B **79**, 205103 (2009).
[39] See Supplemental Material at http://link.aps.org/supplemental/10.1103/PhysRevB.90.075134 for the band structure, density of

states, atom charges and magnetic moments, Fe-O bond length distributions, NMR frequencies, and relaxed Fe-Fe distances.

[40] J. A. Weil, J. R. Bolton, and J. E. Wertz, *Electron Paramagnetic Resonance: Elementary Theory and Practical Applications* (Wiley, New York, 1994).

[41] G. Mallia, R. Orlando, C. Roetti, P. Ugliengo, and R. Dovesi, Phys. Rev. B **63**, 235102 (2001).

[42] A. Kramida, Yu. Ralchenko, J. Reader, and NIST ASD Team, NIST Atomic Spectra Database (version 5.1), http://physics.nist.gov/asd.

[43] L. R. Bickford, Phys. Rev. **78**, 449 (1950).

[44] C. Kittel, Phys. Rev. **76**, 743 (1949).

[45] V. N. Sharma, J. Appl. Phys. **36**, 1450 (1965).

[46] R. Dovesi, V. R. Saunders, C. Roetti, R. Orlando, C. M. Zicovich-Wilson, F. Pascale, B. Civalleri, K. Doll, N. M. Harrison, I. Bush *et al.* (2009), CRYSTAL09 user's manual, University of Torino, Torino, Italy, 2009.

[47] A. D. Becke, Phys. Rev. A **38**, 3098 (1988).

[48] P. S. Bagus and B. Liu, Phys. Rev. **148**, 79 (1966).

[49] P. S. Bagus, B. Liu, and H. F. Schaefer, III, Phys. Rev. A **2**, 555 (1970).

[50] A. J. Freeman and R. E. Watson, Phys. Rev. Lett. **5**, 498 (1960).

[51] R. E. Watson and A. J. Freeman, Phys. Rev. **123**, 2027 (1961).

[52] W. J. Childs and L. S. Goodman, Phys. Rev. **148**, 74 (1966).

[53] M. Munzarová and M. Kaupp, J. Phys. Chem A **103**, 9966 (1999).

[54] L. Hermosilla, P. Calle, J. M. Garcia de la Vega, and C. Sieiro, J. Phys. Chem. A **109**, 1114 (2005).

[55] Y. Zhang, A. Castets, D. Carlier, M. Ménétrier, and F. Boucher, J. Phys. Chem. C **116**, 17393 (2012).

[56] M. Catti, G. Valerio, and R. Dovesi, Phys. Rev. B **51**, 7441 (1995).

[57] M. D. Towler, N. L. Allan, N. M. Harrison, V. R. Saunders, W. C. Mackrodt, and E. Aprà, Phys. Rev. B **50**, 5041 (1994).

[58] H. Monkhorst and J. D. Pack, Phys. Rev. B **13**, 5188 (1976).

[59] A. D. Becke, J. Chem. Phys. **98**, 5648 (1993).

[60] P. J. Stephens, F. J. Devlin, C. F. Chabalowski, and M. J. Frisch, J. Phys. Chem. **98**, 11623 (1994).

[61] P. A. M. Dirac, Proc. Cambridge Philos. Soc. **26**, 376 (1930).

[62] C. Lee, W. Yang, and R. G. Parr, Phys. Rev. B **37**, 785 (1988).

[63] S. H. Vosko, L. Wilk, and M. Nusair, Can. J. Phys. **58**, 1200 (1980).